

Snow cover prediction in the Italian Central Apennines using weather forecast and snowpack numerical models

Edoardo Raparelli^{1, 2}, Paolo Tuccella^{3, 2}, Valentina Colaiuda^{3, 2}, and Frank S. Marzano^{1, 2}

¹Dept. Information Engineering, Electronics and Telecommunications, Sapienza Università di Roma, Italy

²Center of Excellence Telesensing of Environment and Model Prediction of Severe Events (CETEMPS), L'Aquila, Italy

³Dept. Physical and Chemical Sciences, Università degli Studi dell'Aquila, Italy

Correspondence: Edoardo Raparelli (edoardo.raparelli@uniroma1.it)

Abstract.

Italy is a territory characterized by complex topography with the Apennines mountain range crossing the entire peninsula with its highest peaks in central Italy. Using the latter as area of interest and the winter seasons 2019, 2020 and 2021, the goal of this study is to investigate the ability of snow cover models to reproduce the observed snow height, using forecast weather data as meteorological forcing. We here consider two well-known ground surface and soil models: i) Noah LSM, a single-layer Eulerian model; ii) Alpine3D, a multi-layer Lagrangian model. We adopt the Weather Research and Forecasting (WRF) model to produce the meteorological data to drive both Noah LSM and Alpine3D at regional scale with a spatial resolution of 3 km. While Noah LSM is already online coupled with the WRF model, we develop here a dedicated offline coupling between WRF and Alpine3D. We validate the WRF simulations of surface meteorological variables in central Italy using a dense network of automatic weather stations, obtaining correlation coefficients higher than 0.68, except for wind speed which suffered of the model underestimation of the real elevation. The performances of both WRF-Noah and WRF-Alpine3D, are evaluated by comparing simulated and measured snow height, snow height variation and snow water equivalent, provided by a quality-controlled network of automatic and manual snow stations located in Central Apennines. We find that WRF-Alpine3D can predict better than WRF-Noah the snow height and the snow water equivalent, showing a correlation coefficient with the observations of 0.87 for the former and 0.74 for the latter. Both models instead show similar performances in reproducing the observed daily snow height variation, nevertheless WRF-Noah is slightly better to predict large positive variations, while WRF-Alpine3D can slightly better simulate large negative variations. Finally we investigate the abilities of the models in simulating the snow cover area fraction, and we show that WRF-Noah and WRF-Alpine3D have almost equal skills, with both models overestimating it. The equal skills are also confirmed by Jaccard and the Average Symmetric Surface Distance indexes.

20 1 Introduction

Snow cover is a key element within global and local climate due to its high reflectivity of solar radiation and thermal insulation effects of land surfaces, inducing a non linear feedback in the Earth energy balance (Hall, 2004). Snowpack melting is an essential water supply to sub-surface reservoirs, urban populations and agricultural activities which mainly rely on frozen water stored in the snowpack (Barnett et al., 2005). For mountainous touristic places the persistence of snow cover is the basis

25 of their winter sport economy (Vanat, 2020). Nevertheless, the snowpack can be potentially dangerous when sliding down a slope causing avalanches with possible major damages to local flora, fauna and even human settlements (Bebi et al., 2009).

The simulation of the seasonal snow cover is particularly challenging in mountainous regions because of the complex interaction between atmospheric flow and topography. Indeed the synoptic flow approaching the topography may lead to the formation of local phenomena, like orographic precipitation, that have a large influence on snow deposition patterns and evolution. Also smaller scale phenomena, like local cloud formation, preferential deposition and snow redistribution can cause large snow cover variations within few meters (Mott et al., 2018).

Also small scale phenomena, like wind erosion or accumulation (Sommer et al., 2018) and preferential deposition (Lehning et al., 2008), can cause large snow cover variations within few meters. Thus the quality of a distributed simulation of the snow cover is closely related to the horizontal resolution and the quality of the atmospheric data used to force the snow cover model.

35 Recently the use of numerical weather prediction (NWP) models to drive snow cover models have become more and more investigated, thanks to the improved computer performances allowing to increase the spatial resolution and decrease the computational time. Bellaire et al. (2011), Bellaire et al. (2013) and Bellaire and Jamieson (2013) simulated the snow cover properties over British Columbia with the SNOWPACK model (Bartelt and Lehning, 2002; Lehning et al., 2002a, b), forced with atmospheric data provided by the the NWP model GEM15 (Mailhot et al., 2006), suggesting the possibility to force snow cover models with simulated weather data where observations are not available, and showing promising results on the possibility of predicting critical layers formation. Still in western Canada, Schirmer and Jamieson (2015) showed that forcing SNOWPACK with the NWP model GEM-LAM (Erfani et al., 2005) at 2.5 km resolution provided better results than using the GEM15 model, because of its higher resolution. Moreover, Horton et al. (2015) and Horton and Jamieson (2016) investigated the dependency of surface hoar formation on local meteorological and terrain conditions and the possibility to predict it driving SNOWPACK with the GEM-LAM model. Vionnet et al. (2016) simulated the snowpack evolution over the French Alps driving the snow cover model Crocus (Vionnet et al., 2012) with the NWP model AROME (Seity et al., 2011), and Quéno et al. (2016) applied the same model chain on French and Spanish Pyrenees. Bellaire et al. (2017) used SNOWPACK forced with the NWP model COSMO (Doms and Schättler, 2002) to forecast wet snow avalanche activity on the Swiss Alps. Vionnet et al. (2017) forced Crocus with the NWP model Meso-NH (Lafore et al., 1997) at 50 meter resolution, showing that for their case study in the French Alps, snow eolian transport is the main cause of snow height variability. Gerber et al. (2018) compared COSMO-WRF simulations (Skamarock et al., 2008) from 135 m to 50 m resolution over the Swiss Alps to radar estimations, and highlighted that in presence of complex terrain a good representation of the topography is essential to predict the observed snow precipitation and accumulation variability. Luijting et al. (2018) forced Crocus model with AROME-MetCoOp forecasted data (Müller et al., 2017) and a combination of AROME-MetCoOp and GridObs data (Lussana et al., 2018b, a) in southern Norway, and showed that bias in GridObs data due to not homogeneous distribution of AWS at different elevations affects the snowpack simulation, causing an early melt of the snow cover at high elevations. Vionnet et al. (2021) combined the High-Resolution Deterministic System (HRDPS; Milbrandt et al. (2016)) and the Canadian Hydrological Model (CHM; Marsh et al. (2020b, a)), which allows for explicit snow redistribution modelling, and showed that the blowing-snow and gravitational snow redistribution are necessary to reproduce the spatial variability of snowpack in alpine terrain. Lastly, Sharma et al. (2021) online

60 coupled WRF and SNOWPACK, and introduced a new blowing snow scheme. In this configuration, WRF drives SNOWPACK which acts as land surface model and gives feedback to WRF. This permits to simulate a large number of snow layers, and thanks to the blowing snow scheme even snow erosion and redistribution can be simulated, as they showed for case studies in Antarctica and Swiss Alps.

Most of the cited works are focused on higher latitude and altitude mountain ranges, like the Canadian mountains, European Alps or Pyrenees, which have many peaks above 3000 m, or on cold regions like Antarctica. So far no study focused on lower latitude mountain ranges with peaks below 3000 m, such as the Italian Apennines. The latter is a series of mountains, bordered by narrow coastal lands, forming a great arc along the Italian peninsula, from the Maritime Alps down to the Egadi Islands in western Sicily. Their total length is about 1400 km and their width goes from about 40 to 200 km. Their eastern slopes down to the Adriatic Sea are typically steeper and more verdant than the western ones. As a matter of fact, the Apennines play a significant role in the Italian climate being a natural topographic barrier to both western Atlantic cyclonic fronts and eastern cold air intrusions, causing intense snowfalls and hazardous avalanche activity (Chiambretti and Sofia, 2018), which may lead to fatal tragedies (Frigo et al., 2021). Its highest peak is the mount Corno Grande (2912 m) in the Gran Sasso chain in central Italy, belonging to the Central Apennines, in the Abruzzo region. The Gran Sasso is also hosting the southernmost European paraglacier (glacial apparatus), named Calderone, a key sentinel of current climate change in the Mediterranean region. Due to its complex topography and relatively low altitudes, the Apennines snow cover monitoring and forecast are quite cumbersome and, to some extent, open further issues with respect to high altitude mountainous regions.

The aim of this study is to investigate the ability of two snow cover numerical models to reproduce the observed snow height in Central Apennines, using forecast weather data as meteorological forcing. To this purpose, we use two well-known snow and soil models: i) Noah LSM, a single-layer Eulerian model (Chen and Dudhia, 2001); ii) Alpine3D, a multi-layer Lagrangian model (Lehning et al., 2006). We adopt the Weather Research and Forecasting (WRF) model to produce the meteorological data to drive both Noah LSM and Alpine3D at regional scale with a spatial resolution of 3 km.

While Noah LSM is already online coupled with the WRF model, we develop here a dedicated offline coupling between WRF and Alpine3D for the first time, at least to the best of the authors knowledge. The offline coupling of the two models gives the opportunity of running just Alpine3D in the case WRF simulations have already been performed. This is particularly useful if different parametrizations have to be tested in Alpine3D only and not in WRF. Moreover, the offline coupling of WRF and Alpine3D may be easily used by the services that already uses WRF operationally, by just installing Alpine3D and the interfacing library, without the need of modifying the already present WRF configuration. Nevertheless, it is important to note that the offline coupling of Alpine3D and WRF can be extended to other NWP models, just making small modifications to the interfacing library.

By means of the two numerical models WRF-Noah and WRF-Alpine3D, we simulate the snowpack evolution over the Italian Central Apennines for three winters, from December 2018 till April 2021, and compare the snow cover forecast results with in situ measurements of snow height, snow water equivalent and satellite-based radiometric observations of snow extent.

The present paper is structured as follows. In Sect. 2 we provide a brief description of the climate of the area of interest and a synoptic view of the three chosen winters. In Sect. 3 we describe the observations data set, the atmospheric model and the

95 two snow cover models, as well as the built numerical model chain. We then introduce the statistical indices used to evaluate the model skills. Finally, in Sect. 4 we compare and discuss observed and simulated data in terms of: i) atmospheric forcing, ii) snow height, iii) snow water equivalent iv) snow cover extent. Conclusions are drawn in last section.

2 Area and period of interest

In this section we first introduce the climatology of Italian Central Apennines with a view on the synoptic characteristics for
100 winters 2019, 2020 and 2021.

2.1 Climatology of Italian Central Apennines

From a climatological point of view, inner central Italy is classified as Cfb, according to the Köppen system (Köppen, 1931; Pinna, 1970; Belda et al., 2014). As a part of the Mediterranean region, the climate in this area of the Italian peninsula is characterized by alternating rainy periods in winter months and dry periods during Summer. In general, the temperature excursion,
105 on daily and annual basis, does not exceed 21°C, due to the mitigating effect of both the Tyrrhenian and the Adriatic seas that surround a quite narrow strip of land, with an average width of 240 km in W-E direction. Besides, due to its complex topography and elevations ranging from 0 to 2914 m a.s.l. (Corno Grande peak), in an extension of few tens of kilometres, the area is also characterized by a high micro-climatic variability, from meso-Mediterranean to sub-continental temperate, in the inner part, close to the highest peaks of the Apennines ridge (Lena et al., 2012).

110 According to the statistics provided by Report no. 55 of the Italian Institute for Environmental Protection and research (ISPRA, 2015) the annual average temperature in Central Italy ranged from 5°C (mountain areas) to 20°C (coastal area) in the reference period 1981-2010. The minimum and maximum temperature values are encompassed between 3°C and 11 °C and between 8°C and 22°C, respectively. Annual average accumulated precipitation is estimated to be between 600 and 1500 mm, being the yearly maxima mainly localized in the western slope of the Apennine mountain range, exposed to the Tyrrhenian Sea.
115 Minimum precipitation values occur over both the western and eastern littoral areas. Summer coincides with the dry period, when accumulated precipitation ranges between 40 to 80 mm. In this context, it is worth mentioning as the average annual temperature and precipitation reported in the Central Apennines area are 3.7 °C (-8.9 °C the mean minimum temperature) and 1170 mm, respectively (Petriccione and Bricca, 2019).

In Central Apennines, the precipitation maxima are reached in Autumn and Spring and no drought period occurs during
120 summer. As for the snow, mean solid precipitation depth (historical data from 1921 to 1960) on an annual basis ranged from 0-5 cm on the Tyrrhenian littoral area to a maximum value 100-300 cm on the Apennines (Ministero dei Lavori Pubblici, 1973). Eastern slope and Adriatic side was found to have a greater average amount of snow, with climatological values up to 20-50 cm in the coastal zone. Accordingly, the estimated number of chill days ranged from a minimum value of 0-1 in the western coast, to 150-200 days in the inner part (Ministero dei Lavori Pubblici, 1973).

125 As observed by [Libertino et al. \(2018\)](#); [Rossi \(2020\)](#); [Alberton \(2021\)](#), after 1970s, the fragmentation of the National Hydrographic Service into twenty different regional offices (one per Italian region) led to the loss of homogeneity in meteorological

data collection and statistics. While several studies are available in the Alps and northern Italy, central and southern Italy suffer from a poorly densed snow gauges network. Nevertheless, since central Apennines are particularly prone to avalanche hazards, which has caused frequent casualties in the last few years, some authors have focused their attention on the occurrence of extreme snowfall events. In the last decades, Piacentini et al. (2020) observed a decrease in snowfall, snow cover and snow persistence over the area, although a few extreme snowfall events were recorded. High snow occurrence/accumulation variability of this part of Italy is also highlighted by Fazzini et al. (2021). Several authors have highlighted a decreasing trend in winter precipitation in Central Italy in recent decades (Brunetti et al., 2000; Pavan et al., 2008; Longobardi and Villani, 2010; Romano and Preziosi, 2013; Appiotti et al., 2014; Scorzini and Leopardi, 2019). In the Gran Sasso d'Italia massif, the Inter-regional Association for coordination and documentation of snow and avalanche problems (AINEVA), records a decreasing number snow days on altitudes below 1300 m a.s.l, in the 30-year period 1978-2007, even if events with intense snowfalls are increasing in some specific areas (Romeo and Massimiliano, 2008).

2.2 Synoptic view

2.2.1 2018-2019

Winter 2018-2019 may be divided into three phases, from a synoptic point view. During December, the Euro-Mediterranean area was characterized by a strong positive 500 hPa geopotential height anomaly centered on the Iberian Peninsula, whilst a near neutral, or slightly negative, geopotential anomaly affected Eastern Europe. This resulted in a warm and dry pattern over the Western Mediterranean basin. By contrast, in January an oceanic anticyclonic system with above normal geopotential heights determined a flux of Arctic cold air toward the Mediterranean through Eastern Europe. This generated a generalized cold temperature anomaly over Central and Eastern Europe and Central Mediterranean basin, with associated above normal precipitations over Central and Eastern Mediterranean Sea. Finally, February was dominated by a robust 500 hPa geopotential height anomaly extended to the whole continental Europe. As a result, the Euro-Mediterranean region was characterized by warm temperatures and dry conditions.

This pattern affected the precipitations in central Italy as follows. Between 10th and 20th December, the circulation over Central Italy was affected by geopotential negative anomalies centred on Eastern Europe. In the middle of December, cold air advection from Northern and Northern-Eastern Europe led to snowfall down to 700 m a.s.l., and the snowpack height measured at the observational sites ranged from 15 to 50 cm. During the second part of the month, the atmospheric conditions were influenced by the positive geopotential anomaly localized on the Iberian Peninsula. The associated mild weather caused a consistent lowering of snow height, especially at the middle and low altitude sampling sites.

The most important snowstorm of the season occurred between 2nd and 4th January 2019, which resulted in an observed snow height in the range of 20-100 cm. Snowpack height did not show larger variations up to 22nd January, due to the low temperatures and minor snowfall events. Between 23rd and 24th January, thanks to cold air advection from North Atlantic, a mean of 40 cm of fresh snow was observed at our measurement sites.

An average lowering of 30 cm of the snow height was observed between 1th and 3rd February, due to a warm advection over
160 Italy from North Africa. The rest of the month was characterized by a slow decay of snow height, due to general mild and dry
atmospheric conditions.

2.2.2 2019-2020

Winter 2019-2020 was not favourable to a formation of a consistent snowpack. The Western Mediterranean basin was domi-
nated by an extended positive geopotential height anomaly. Due to the mild and dry conditions resulting from this circulation
165 pattern, only minor snowfall events occurred with the formation of a very thin snow cover at the highest elevation of our do-
main. This synoptic configuration has been unblocked in March that was characterized by a normal 500 hPa circulation with
temperatures slightly under the average and precipitation above the climatology on Central Italy. The most important snow
storm occurred at the end of March, when the snowpack reached a maximum height of 10-80 cm at our observational sites. The
snowpack lowered immediately after the accumulation phase due to the warm relative warm spring conditions and vanished
170 before the middle of April.

2.2.3 2020-2021

Winter season 2020-2021 may be divided in three phases. During December and January, Europe was subjected to strong
negative 500 hPa geopotential height anomalies, resulting in wet conditions on our domain with in near average temperatures
in December and cold conditions in January. By contrast, February was dominated robust anticyclonic on which involved
175 the Mediterranean resulting in mild weather but with near normal precipitation rate on our domain. Finally, March presented
positive 500 hPa geopotential height anomalies on British Isles which determined a cold air flux from Russia direct toward the
Mediterranean, but with below normal precipitation on our domain of study.

The snowpack began to form at the end of November and remained on relatively thin heights up to the end of December.
Starting from the end of 2020, a series of snowfall events interested our domain until the end of January. In this period, the snow
180 height ranged from 30 to 150 cm. In February, the snowpack height decreased due to the average warm conditions, although an
important snow storm occurred in the middle of the month. In March, a series of important snowfalls reported the snow height
up to 100-150 cm.

3 Data, models and evaluation methods

In this section we present the observational data, we describe the considered atmospheric and snow cover models and finally
185 we define the performance evaluation methods.

3.1 Observational data set

The observational data set consists of in situ measurements of atmospheric and snow cover conditions, coming from automatic
weather stations (AWS), manual measurements as well as of snow cover extent derived from satellite-based observations.

The in situ measurements come from a dense network of 730 measurements sites which covers the entire study area. The measurement sites consist of 703 AWS maintained by the Italian Civil Protection (Italian Civil Protection Department and CIMA Research Foundation, 2014), and 27 snow fields maintained by the Meteomont service (Rapisarda and Pranzo, 2021) (Fig. 1b). The variables provided by the AWS are near-surface air temperature ($^{\circ}\text{C}$), relative humidity (%), wind speed (ms^{-1}), incoming shortwave radiation (Wm^{-2}), precipitation (mm) and snow height (cm), while manual measurements provide snow height (cm) and bulk snow density (kgm^{-3}), which we used to derive also the snow water equivalent (kgm^{-2}). Table 1 shows the number of measurement sites providing the above variables. The AWS have an acquisition interval ranging between 15 minutes and 1 hour and they are sent to the Italian Civil Protection server every 15 minutes. We daily averaged all observed variables, with the exception of precipitation which we accumulated over one day, in order to set a common temporal framework. The snow height measurements are carried out with automatic ultra-sonic sensors, installed on 13 weather stations and located along the Italian Central Apennines. Manual measurements instead are performed almost once per day every day for each Meteomont site, however the measurement frequency for winter 2020 and 2021 was drastically reduced because of the difficulties related to COVID-19 pandemic.

Daily snow cover fraction is obtained from MODIS Terra imaging sensor (product MOD10A1 (Metsämäki et al., 2012)). We used 275 maps of snow cover fraction covering winters 2019, 2020 and 2021. We first process MODIS maps in order to obtain cloud-free snow cover fraction maps as follows: the pixels classified as clouds are masked, and for each cloud pixel a linear interpolation between previous and consecutive images is carried out where the pixels are not cloud covered, in order to infer their fractional snow cover area. Then we regridded the cloud-free snow cover fraction maps on a regular grid of resolution 3 km.

In this section, we first introduce the weather forecast model, adopted and tuned to the study area of this work, as well as the two snow cover models, specifically Noah LSM and Alpine3D. In the methodological paragraph we describe the error indices used to quantitatively evaluate the error statistics when comparing both WRF-Noah and WRF-Alpine3D with observational data.

3.2 Description of numerical models

The atmospheric and snow cover numerical models are here briefly described, highlighting the space-time set up and main physical parameterizations employed in this study.

3.2.1 Weather Research and Forecasting (WRF) model

The Weather Research and Forecasting (WRF) model is used in this work to describe the atmospheric evolution at mesoscale. WRF is a regional non-hydrostatic meteorological model including several options for the parameterizations of atmospheric physical processes (Skamarock et al., 2008). As shown in Fig. 1a, the WRF atmospheric model is configured with three two-way nested domains. The largest domain has a 27 km spatial resolution and the second domain has 9 km spatial resolution, whereas the inner domain has a cloud-resolving module at 3 km resolution. The vertical grid is constituted by 33 vertical levels extending from surface up to 50 hPa (about 20 km above the sea level) with the first level at 10 m from the surface.

The WRF main parameterizations include: i) the Yonsei University (YSU) scheme for the planetary boundary layer (Hong et al., 2006); ii) the Rapid Radiative Transfer Model for General circulation model (RRTMG) for visible and infrared radiation (Iacono et al., 2008); iii) the Thompson scheme for cloud microphysics (Thompson et al., 2008); iv) the Grell-Freitas for cumulus convection (Grell and Freitas, 2014) with exception for the cloud-resolving domain, where no cumulus parameterization is activated. The land cover classification used in WRF is based on the 20 classes MODIS scheme. Initial conditions for WRF were taken from 6-hourly operational NCEP analyses at a resolution of 27 km, whilst for the nested domains, boundary conditions are derived from domain 1 and 2 simulations, respectively. In order to improve the meteorological simulations, a spectral nudging toward NCEP analysis of wind, temperature, and geopotential is applied in the outer domain above 850 hPa. With exception of the first simulation of this series, the land surface and soil properties are restarted by using the previous meteorological prediction in order to avoid a discontinuous simulation of the snowpack in the study area. We have chosen this setup for WRF because it revealed to be the best in simulating the main observed meteorological variables according to many preliminary sensitivity tests that we carried out.

3.2.2 Noah Land Surface Model

Within the WRF model, land surface processes are simulated with the Noah LSM (Chen and Dudhia, 2001). Noah LSM is a model that simulates skin temperature, snow height, snow water equivalent, snow density, soil moisture, soil temperature and surface energy balance. The snowpack is represented as a single layer of varying thickness, instead the soil is discretized in four layers of thickness 10, 30, 60 and 100 cm respectively. Noah LSM is online coupled with WRF, and it provides to the parent model surface and latent heat fluxes, and upward shortwave and longwave radiation. The improvements in the Noah snowpack model introduced by Livneh et al. (2010) and Wang et al. (2010) were taken into account in our simulations. The WRF-Noah model is run separately for the winters 2019, 2020 and 2021, and for each season we started the simulations several days before the first snowfall occurred in all the considered measurement sites.

3.2.3 Alpine3D snow and soil model

Alpine3D is a three-dimensional snow cover, land surface and soil numerical model (Lehning et al., 2006). It includes the one-dimensional model SNOWPACK (Bartelt and Lehning, 2002; Lehning et al., 2002a, b) to simulate snow, land surface and soil properties, the SnowDrift module to simulate the wind transport of snow, the EBalance module to compute radiation fields taking into account topographic shading and reflections effects and a runoff module. SNOWPACK is the core of Alpine3D, it is developed using a Lagrangian scheme which permits to provide detailed description of snow stratigraphy, mass and energy balance, simulating up to 50 snow layers. In order to run an Alpine3D simulation, it is necessary to provide the initial state of snow and soil (if soil simulation is enabled), a digital elevation model, a land cover model and a meteorological input.

Alpine3D is not coupled with WRF so that it is necessary to interface the two models. The digital elevation model and the land cover model, used in the Alpine3D simulation, are the same extracted from the WRF model. We have enabled in Alpine3D the soil simulation, creating 4 soil layers of 10, 30, 60 and 100 cm respectively, and initialized them using the soil condition extracted from WRF. For each year, Alpine3D is initialized with snow-free conditions on each grid cell. To drive Alpine3D,

255 we use the air temperature, relative humidity, wind speed, incoming shortwave radiation, incoming longwave radiation, total precipitation, precipitation phase and ground surface temperature extracted from WRF. WRF-Alpine3D hourly maps of snow height and snow water equivalent are then generated for the whole period. All the data used to drive Alpine3D have been re-projected on a regular grid of 3 km resolution, since the WRF curvilinear grid is not supported by Alpine3D. A scheme of the described WRF-Alpine3D model chain is shown in Fig. 2.

260 In our Alpine3D simulation setup, we turn off the SnowDrift and the EBalance modules: indeed, at the resolution of 3 km the wind transport of snow and the topographic shading and reflections effects have a negligible impact on the simulation results. We enabled the canopy representation in Alpine3D. After a sensitivity test (not shown here), we opted for neutral atmospheric stability conditions for turbulent fluxes estimation as well as "Zwart" and "Lehning_1" parametrizations for new snow density and snow albedo respectively. Even if more computational demanding, we use the Richards water transport scheme instead of
265 the more simple bucket scheme, because it improves the performance of the model to estimate the meltwater runoff (Wever et al., 2014).

3.3 Performance evaluation indices

We here distinguish the error indices for atmospheric variable and snow height prediction from those used to estimate the discrepancy in the snow cover extension.

270 WRF skill in predicting the meteorological variables is evaluated comparing the output with in situ observations. The simulated air temperature, relative humidity, wind speed, incoming shortwave radiation and precipitation are bilinearly interpolated on the coordinates of the observed data. They are daily averaged, with the exception of precipitation rate which is accumulated over one day. The simulated variables are statistically evaluated using mean bias error (MBE), mean absolute error (MAE) and Pearson correlation coefficient (R) for three elevation bands (low elevation: < 800 m, mid elevation: 800-1600 m, high
275 elevation: ≥ 1600 m).

From the manually measured snow height and snow density we derive snow water equivalent (SWE), which is defined as:

$$\text{SWE} = \rho_s h_s \quad (1)$$

where ρ_s is the snow density in kgm^{-3} and h_s is the snow height in meters. The simulated snow height and snow water equivalent are bilinearly interpolated on the coordinates of the in situ observations, and then re-sampled at a temporal resolution
280 of one day. Starting from daily snow height, we derive the corresponding daily variations. In order to evaluate the model-based simulations of snow height, snow-height variation and snow water equivalent, we use again MBE, MAE and R. For the snow height variation, the Equitable Threat Score index (ETS) is also used (as proposed by Nurmi (2003) and Schirmer and Jamieson (2015)), and quantify the model skill in hitting a binary observation, like snow height exceeding a certain threshold.

The skill of WRF-Noah and WRF-Alpine3D model in reproducing the snow cover extent observed with MODIS are also
285 evaluated. To this end, snow cover fraction maps are obtained for both WRF-Noah and WRF-Alpine3D from the following equation, equivalent to the empirical relation found by Koren et al. (1999):

$$F_s = 1 - \left(e^{-\alpha_s (W_s / W_{max})} - \frac{W_s}{W_{max}} e^{-\alpha_s} \right) \quad (2)$$

where $\alpha_s = 2.6$ is a distribution shape parameter, W_s is the simulated snow water equivalent, W_{max} is the snow water equivalent threshold above which the soil is 100% covered with snow, and varies locally according to MODIS land use classification. While Noah LSM already calculates the snow cover fraction according to Eq. 2, Alpine3D doesn't, thus we had to calculate it a-posteriori using Eq. 2. By applying a threshold of 51%, we can build binary maps which indicate: i) snow absence if snow cover fraction is below the threshold; ii) snow presence if snow cover fraction area was equal or above the threshold. These binary maps are compared by using the Jaccard index (J) and the average symmetric surface distance (ASSD). The J index is equal to 1 if the binary maps perfectly overlap, instead is equal to 0 if they don't overlap. The ASSD index ranges from 0 to ∞ , and 0 means perfect overlap of the boundaries of the binary maps. The application of ETS, J and ASSD to snowpack model validation is clearly described by Quéno et al. (2016).

From the snow cover binary maps of MODIS, WRF-Noah and WRF-Alpine3D we finally calculate the respective snow cover area fraction, which is defined as the number of cells classified with snow divided by the total number of cells of the study domain. We compare the simulated snow cover area fractions with the one obtained from MODIS and we evaluate them in terms of MBE, MAE and R.

4 Results and discussion

Both models, WRF-Noah and WRF-Alpine3D, are compared with observational data for the study area for winter 2019, 2020, 2021. The performance analysis is carried out in terms of the error indices, defined in the previous section, for both atmospheric and snow cover forecast.

4.1 Performance analysis of the atmospheric model

As a first validation, Figure 3 shows the scatter plots of the comparison between simulated and measured daily air temperature, relative humidity, wind speed and incoming shortwave radiation and daily precipitation. The colors represent the observation density for each pixel, the brighter the color, the higher the density of observations for that pixel. The statistical scores, obtained from this intercomparison, are reported in Table 3 for the three elevation ranges defined in Section 3.3 and for all altitudes.

WRF presents for the air temperature at all elevation ranges a correlation coefficient higher than 0.89, with an overall score of 0.9 (Fig. 3a). The WRF simulations exhibit a slightly negative MBE, especially for elevations between 800 m and 1600 m, where it also shows the highest MAE.

The relative humidity presents a correlation coefficient higher than 0.76 for mid and high elevation bands but lower (0.68) for low elevations, with an overall score of 0.68 (Fig. 3b). The MBE and the MAE increases with the altitude.

From Fig. 3c we note that that WRF in some cases drastically underestimates the wind speed. These points correspond to high elevations measurement sites. Indeed at low elevations WRF shows a positive MBE, which decreases and becomes negative as the elevation increases. Clearly, also the MAE show an elevation dependence, and increases from low to higher altitudes. Moreover, the correlation coefficient is minimum at high elevations and maximum at low elevations. The wind speed

underestimation at high elevation is due to an underestimated elevation of the topography. Indeed the 3 km resolution of the
320 model simulation smooths the highest peaks, causing to a lower simulated wind speed at station location.

Figure 3d shows that WRF overestimates the incoming shortwave radiation. At high elevations, WRF has the highest MAE and the lowest correlation with the in situ observations. The general overestimation of incoming shortwave radiation is again partly due to the limited model horizontal resolution. Indeed shading effect that influence the measured solar radiation may not be captured by the model, in which the topography is more smooth and low compared to reality.

325 Figure 3e highlights that WRF reproduces the daily precipitation with a correlation coefficient between 0.77 (for low elevations) and 0.64 (for high elevations). WRF shows the tendency to overestimate the precipitation as the altitude increases. Indeed, the bias is negligible below 800 m of altitude, but MBE reaches more than 4 mm at the high altitude sites. This overestimation is likely due to the fact that rain gauges typically lose a precipitation fraction. When the precipitation is solid the underestimation is even larger because part of it is lost with sublimation, especially when the rain gauge is not heated.

330 In summary, for the WRF-simulated variables the overall correlation coefficient is above 0.68, except for the wind speed, because as we already discussed, the strong negative bias at high elevations decreases the overall correlation to 0.49. On the other hand, it is well known that the wind speed field is particularly variable in complex orographic regions and a point-like in situ measurement cannot be representative of 3 km spatially averaged wind speed at WRF model scales considered in this study.

335 4.2 Performance analysis of snow cover models

4.2.1 Snow height

The time series intercomparison can be useful to show the temporal behaviour of the two models with respect to in situ observations. The first row of Fig. 4 shows the median of the snow height observed and simulated at all the AWS sites. Observations are indicated by a dashed gray line, while the numerical simulations are indicated by solid blue and red lines,
340 corresponding to WRF-Noah and WRF-Alpine3D respectively. The shaded areas correspond to the interval comprised between minimum and maximum observed and simulated snow height. For winter 2018-2019 this comparison indicates that the snow height, simulated by the two models, is similar until mid January, but during the last part of the winter, WRF-Alpine3D better reproduces the observed snow height, also in terms of settlement rate, while WRF-Noah underestimates the snow height, showing a faster settlement rate. Instead for winters 2019-2020 and 2020-2021, the snow heights simulated with WRF-Noah
345 and WRF-Alpine3D almost overlap. However for every winter in can be noticed that when the melting period begins, WRF-Noah largely underestimates the maximum snow height observed at the measurement sites, while WRF-Alpine3D has a better skill to capture the observed snow height variability between the measurement sites, simulating a maximum snow height more close to the observations.

Another comparison of simulated and observed snow height is shown in the scatter plot of Fig. 5a, which reports the median
350 of observed and simulated values for all the elevation bands shown in Table 2, with blue and red dots indicating WRF-Noah and WRF-Alpine3D respectively. The plot shows that WRF-Alpine3D reproduces with more accuracy the snow height, especially

when the observed snowpack is particularly thick. This results in a much higher correlation coefficient of WRF-Alpine3D compared to WRF-Noah (0.87 and 0.68 respectively) and in a negative bias of WRF-Noah in the snow height estimation (see Table 4 for all evaluation indices).

355 Snow height variation is an important indicator of the models skill to catch the dynamical behavior of the snow cover. Thus we compared simulated and observed snow height variations and we evaluated the model performances in terms of MBE, MAE and R. The results are shown in Table 4. In this case WRF-Alpine3D doesn't present better skills compared to WRF-Noah, indeed the models present almost the same correlation coefficient and MAE. A slightly difference between the models can be seen in the MBE which is slightly negative for WRF-Noah and positive for WRF-Alpine3D.

360 A more detailed view of the skill of WRF-Noah and WRF-Alpine3D in calculating the observed daily snow height variation comes from the analysis of Fig. 6a and 6b. Figure 6a shows the observed and modelled frequency distribution of daily snow height variation at the 13 validation sites used in this study. Grey column represents the observed variations and the blue and red columns represent the snow height variations simulated with WRF-Noah and WRF-Alpine3D, respectively. For the range of variations between [-20 cm, +30 cm[, WRF-Noah and WRF-Alpine3D show similar performances, simulating a number
365 of snow height variations for each class similar to the observations. Outside of this range, the behaviour of the two models is clearly different. Below -20 cm, WRF-Alpine3D shows a better skill in reproducing the observed snow height variation, indeed variations in the interval [-30 cm, -20 cm[are totally missed from WRF-Noah. Instead for variations larger than 30 cm WRF-Noah seems to be more accurate to reproduce the observations compared to Alpine3D. The snow height variations observed in the range [40 cm, 50 cm[are not captured by both WRF-Noah and WRF-Alpine3D. Therefore, both models can
370 well predict the central tendency of the distribution of the daily snow height variation, whereas they have more difficulties on the tails of the distribution. A further confirmation of this behaviour comes from Fig. 6b, where the ETS index for different snow thresholds is reported. A look at Fig. 6b shows again that WRF-Noah and WRF-Alpine3D has similar scores between -1 cm ad 20 cm thresholds, but they perform differently outside of this range. Indeed, compared to WRF-Alpine3D, WRF-Noah shows higher performances for snow height variations larger than 30 cm, however both models do not capture snow
375 height variations larger than 40 cm. Instead, for variations smaller than -1 cm we can see that WRF-Alpine3D reaches scores larger than WRF-Noah. This suggests that WRF-Alpine3D has slightly better skills compared to WRF-Noah in predicting the observed snow settlement, indeed is also known that Noah LSM tends to anticipate the complete melt of the snowpack even at 3 km resolution, as Pavelsky et al. (2011) show for Sierra Nevada Mountains, California.

4.2.2 Snow water equivalent

380 Snow water equivalent is a particularly interesting quantity because it represents the amount of mass stored in the snowpack. We derived snow water equivalent data combining manual measurements of snow height and snow density provided by the Meteomont service. The time series of the median snow water equivalent, observed and simulated at all the manual sites, are shown in the second row of Fig. 4 for each of the considered year. Observations are indicated by a dashed gray line, while the numerical simulations are indicated by solid blue and red lines, corresponding to WRF-Noah and WRF-Alpine3D respectively.
385 The shaded areas correspond to the interval comprised between minimum and maximum observed snow water equivalent.

As can be seen from Fig. 4d, WRF-Noah and WRF-Alpine3D have similar performances during December, estimating a snow water equivalent really close to the observations. During January WRF-Alpine3D slightly overestimates the observed snow water equivalent, and WRF-Noah is more close to the observation, however WRF-Alpine3D reproduce with higher accuracy the observed accumulation rate. During February WRF-Alpine3D reproduces better than WRF-Noah not only the snow water equivalent absolute value, but also its trend. Furthermore, from mid February, Alpine3D simulates maximum snow water equivalent values close to the observations, while WRF-Noah largely underestimates them. During winters 2019-2020 and 2020-2021, the manual measurement taken by the Meteomont service have undergone a notable decrease because of the COVID-19 pandemic (Ciotti et al., 2020). The low temporal frequency of the measurements and the non contemporaneity of the observations at different sites make the time series of the median of the observed snow water equivalent noisy and uninformative, thus we decided to not show it in Fig. 4e and 4f. Nevertheless, also for winters 2019-2020 and 2020-2021, WRF-Alpine3D simulates a maximum snowpack thickness much larger than WRF-Noah during the melting period.

Another comparison of simulated and observed snow water equivalent is shown in the scatter plot of Fig. 5b, which reports the median of observed and simulated values for all the elevation bands shown in Table 2, with blue and red dots indicating WRF-Noah and WRF-Alpine3D respectively. The plot shows that WRF-Alpine3D reproduces with more accuracy the snow water equivalent, especially when the observed snowpack is particularly thick. This results in a much higher correlation coefficient of WRF-Alpine3D compared to WRF-Noah (0.74 and 0.47 respectively) and in a negative bias of WRF-Noah in the snow height estimation (see Table 4 for all evaluation indices).

4.2.3 Snow cover extent

MODIS satellite snow product is an essential independent data set to evaluate the skill of WRF-Noah and WRF-Alpine3D to reproduce the observed snow cover area. As already described, MODIS sensor is providing the snow cover fraction (SCF) maps with 500 m resolution. Thanks to the applied cloud-removal algorithm, we have been able to compare the snow cover extent also for the days with high cloud cover fraction.

As an example, Figs. 7a, 7b and 7c show the SCF maps obtained from MODIS, WRF-Noah and WRF-Alpine3D for 17 December 2018, which was one of the days with the largest observed snow cover area in winter 2018-2019. From the SCF maps, by applying a threshold of 51%, we can derive the snow cover area (SCA), as shown in Figs. 7d, 7e and 7f. Forested areas, according to CORINE classification, are superimposed to MODIS, WRF-Noah and WRF-Alpine3D data, in order to qualitatively evaluate their impact on the snow cover area estimation. Snow cover within forested areas is a critical issue for snow mapping due to the forest signature on MODIS visible and near-infrared imagery, as highlighted by Gascoin et al. (2015). This results in an underestimation of the snow cover extent, especially during spring, when the snow is usually present below the forest but not on the trees, where already melted. Thus it cannot be excluded that WRF-Noah and WRF-Alpine3D overestimation of the snow cover area can be partially due to a MODIS underestimation of the snow cover area where forests are present.

Duration of the snow cover is another important parameter, which has direct implications on many aspects, like local climate, water supply and flora and fauna development. Figure 8 shows the observed and modelled snow cover duration maps, obtained

420 counting the number of times that each cell is classified as covered with snow within MODIS, WRF-Noah and WRF-Alpine3D derived SCA maps. Figure 8 also shows the differences between the snow cover duration simulated with WRF-Noah and WRF-Alpine3D and the one obtained from MODIS. The difference between WRF-Alpine3D and WRF-Noah snow duration is also reported. These figures suggest that WRF-Noah and WRF-Alpine3D tend to simulate a longer snow cover duration on the entire Central Apennines mountain range. The best agreement of the numerical models with the satellite-based observations is found at the valley bottoms. By contrast, the largest differences emerge within middle elevation zones, where both WRF-Noah and WRF-Alpine3D simulate a much longer snow cover duration. A closer inspection of Fig. 8d highlights noticeable differences between WRF-Noah and WRF-Alpine3D in the snow cover persistence. WRF-Noah simulates a more persistent snow cover when compared to WRF-Alpine3D over the northern part of Central Apennines, while Alpine3D predicts a longer snow cover duration in the southern part, especially in the Abruzzo region.

430 The snow cover area fraction (SCAF) can be computed over the chosen domain for each day of the study period, dividing the area classified as covered with snow by the total land area. The result of this calculation is reported in Fig. 9 and statistical indices obtained from this comparison are summarized in Table 5. Both models reproduce SCAF with a high correlation coefficient (0.89 and 0.88 for WRF-Noah and WRF-Alpine3D, respectively), but they overestimate the observed SCAF of 0.06. From these evaluations emerges that the two models present almost identical performances in the estimation of the snow cover area fraction. However the SCAF does not take into account where the snow cover is present, and if observed and simulated snow patches are located in different places, the SCAF could be the same between observations and simulations.

Thus, for each day of the study period, we have evaluated J and ASSD spatial indices, which take into account also where the snow patches are located, and we compared the SCA maps derived for WRF-Noah and WRF-Alpine3D with the ones derived from MODIS. J and ASSD time series are reported in Fig. 10 and their average values are summarized in Table 6. For 440 J and ASSD WRF-Noah and Alpine3D exhibit identical mean values, confirming again that they have almost equal skills in reproducing the observed snow cover area.

5 Conclusions

In this paper we have shown the different skills of Noah LSM and Alpine3D models to simulate the snow cover in Italian Central Apennines when forced with WRF atmospheric data during three winters, going from December 2018 to April 2021. 445 The study area is novel to snow cover studies, since most of past works focused on higher latitude and altitude mountain ranges or on cold regions. So far no study focused on lower latitude mountain ranges with peaks below 3000 m, like Central Apennines.

The performances of the WRF model to simulate air temperature, relative humidity, wind speed, incoming shortwave radiation and precipitation have been first evaluated, comparing them to observations derived from a dense network of automatic weather stations. The WRF model is capable to predict the observed atmospheric variables with a correlation coefficient always higher than 0.68, except for the wind speed for which the model bias strongly increases with the altitude. We have also showed that during winter 2018-2019 WRF-Alpine3D is able to predict with higher accuracy compared to WRF-Noah the observed 450

snow height and snow water equivalent, especially during February 2019. In general, during late winter and spring periods, WRF-Alpine3D is able to reproduce the large snow height observed at some measurement sites, as opposed to WRF-Noah which strongly underestimates it. In terms of daily snow height variation, WRF-Noah and WRF-Alpine3D present similar performances, with correlation coefficient slightly larger than 0.6, but still, the former show a negative bias, while the latter a positive bias. The snow models reveal to have also similar skills to predict small daily snow height variations, but WRF-Noah has slightly better performance to reproduce large positive daily variation, while WRF-Alpine3D has higher skills to predict large negative variations.

Both models WRF-Noah and WRF-Alpine3D tend to overestimate the snow cover area fraction, provided by the MOD10A1 MODIS product. They present almost equal performances in the estimation of the snow cover area fraction. Also the comparison of the models through the Jaccard index (J) and the Average Symmetric Surface Distance (ASSD) confirmed the WRF-Noah and WRF-Alpine3D have almost the same skills to predict shape, location and extension of the observed snow cover.

Future work should be oriented to gather further in situ measurements of grain shape and grain size, necessary to quantify the abilities of WRF-Noah and WRF-Alpine3D to reproduce the observed snow microstructure. A way to improve WRF-Noah and WRF-Alpine3D performances would be to increase the horizontal spatial resolution of WRF simulations (e.g., from 3 km down to 1 km), in order to force the snow cover models with more resolved atmospheric data. Increasing the WRF spatial resolution would also justify the activation in Alpine3D of the modules that take into account the aeolian transport of snow, that redistributes the snow between adjacent cells of the domain according to the forecasted wind field, as well as the impact of the local topography on the energy balance through the effects of incoming shortwave radiation shading and long wave radiation increase. The WRF-Alpine3D simulation could also be improved directly assimilating weather radar data in terms of snowfall rate over the study domain in order to provide more realistic snow accumulation patterns. The approach for weather data assimilation, in terms of point-wise nudging or statistical variational techniques, is an interesting open issue.

Author contributions. E.R. carried out WRF-Alpine3D simulations, designed the work and wrote the paper drafts leading the final version, including figures. P.T. carried our WRF simulations and contributed to design the work as well as write and revise the paper. V.C. contributed to the climatological and meteorological description. F.S.M. contributed to design the work as well as to write and revise the paper, managing the SMIVIA project to co-fund the overall activity.

Competing interests. The authors declare that they have no conflict of interest.

Acknowledgements. This work was partially funded by the Italian Space Agency, (Rome, Italy) within the SMIVIA project (contract N. 2021-9-U.0 CUP F85F21001230005). The authors are thankful to Mathias Bavay for the support on SNOWPACK and Alpine3D models, to Rossella Ferretti for the interesting discussions on numerical weather prediction modelling and for providing the computational resources

to run Alpine3D simulations, to Massimo Pecci and Mauro Valt for sharing with us their experience in the interpretation of the snowpack properties. MODIS products are kindly available from NASA National Snow and Ice Data Center and the CORINE land cover data set is
485 freely provided by COPERNICUS.

References

- Alberton, M.: Water Governance in Italy: From Fragmentation to Coherence Through Coordination Attempts, pp. 355–368, Springer International Publishing, Cham, https://doi.org/10.1007/978-3-030-69075-5_15, https://doi.org/10.1007/978-3-030-69075-5_15, 2021.
- Appiotti, F., Krželj, M., Russo, A., Ferretti, M., Bastianini, M., and Marincioni, F.: A multidisciplinary study on the effects of climate change in the northern Adriatic Sea and the Marche region (central Italy), *Regional environmental change*, 14, 2007–2024, <https://doi.org/https://doi.org/10.1007/s10113-013-0451-5>, 2014.
- Barnett, T. P., Adam, J. C., and Lettenmaier, D. P.: Potential impacts of a warming climate on water availability in snow-dominated regions, *Nature*, 438, 303–309, 2005.
- Bartelt, P. and Lehning, M.: A physical SNOWPACK model for the Swiss avalanche warning: Part I: numerical model, *Cold Regions Science and Technology*, 35, 123–145, [https://doi.org/10.1016/S0165-232X\(02\)00074-5](https://doi.org/10.1016/S0165-232X(02)00074-5), 2002.
- Bebi, P., Kulakowski, D., and Rixen, C.: Snow avalanche disturbances in forest ecosystems—State of research and implications for management, *Forest Ecology and Management*, 257, 1883–1892, <https://doi.org/https://doi.org/10.1016/j.foreco.2009.01.050>, <https://www.sciencedirect.com/science/article/pii/S0378112709000851>, disturbances in Mountain Forests: Implications for Management, 2009.
- Belda, M., Holtanová, E., Halenka, T., and Kalvova, J.: Climate classification revisited: From Köppen to Trewartha, *Climate Research*, 59, 1–13, <https://doi.org/10.3354/cr01204>, 2014.
- Bellaire, S. and Jamieson, B.: Forecasting the formation of critical snow layers using a coupled snow cover and weather model, *Cold Regions Science and Technology*, 94, 37–44, <https://doi.org/https://doi.org/10.1016/j.coldregions.2013.06.007>, <https://www.sciencedirect.com/science/article/pii/S0165232X13000840>, 2013.
- Bellaire, S., Jamieson, J. B., and Fierz, C.: Forcing the snow-cover model SNOWPACK with forecasted weather data, *The Cryosphere*, 5, 1115–1125, <https://doi.org/10.5194/tc-5-1115-2011>, <https://tc.copernicus.org/articles/5/1115/2011/>, 2011.
- Bellaire, S., Jamieson, J. B., and Fierz, C.: Corrigendum to "Forcing the snow-cover model SNOWPACK with forecasted weather data" published in *The Cryosphere*, 5, 1115–1125, 2011, *The Cryosphere*, 7, 511–513, <https://doi.org/10.5194/tc-7-511-2013>, <https://tc.copernicus.org/articles/7/511/2013/>, 2013.
- Bellaire, S., van Herwijnen, A., Mitterer, C., and Schweizer, J.: On forecasting wet-snow avalanche activity using simulated snow cover data, *Cold Regions Science and Technology*, 144, 28–38, <https://doi.org/https://doi.org/10.1016/j.coldregions.2017.09.013>, <https://www.sciencedirect.com/science/article/pii/S0165232X17301891>, international Snow Science Workshop 2016 Breckenridge, 2017.
- Brunetti, M., Maugeri, M., and Nanni, T.: Variations of temperature and precipitation in Italy from 1866 to 1995, *Theoretical and Applied Climatology*, 65, 165–174, <https://doi.org/https://doi.org/10.1007/s007040070041>, 2000.
- Chen, F. and Dudhia, J.: Coupling an Advanced Land Surface–Hydrology Model with the Penn State–NCAR MM5 Modeling System. Part I: Model Implementation and Sensitivity, *Monthly Weather Review*, 129, 569 – 585, [https://doi.org/10.1175/1520-0493\(2001\)129<0569:CAALSH>2.0.CO;2](https://doi.org/10.1175/1520-0493(2001)129<0569:CAALSH>2.0.CO;2), https://journals.ametsoc.org/view/journals/mwre/129/4/1520-0493_2001_129_0569_caalsh_2.0.co_2.xml, 2001.
- Chiambretti, I. and Sofia, S.: Winter 2016–2017 snowfall and avalanche emergency management in Italy (Central Apennines)—A review, in: *Proceedings of the International Snow Science Workshop*, pp. 7–12, 2018.
- Ciotti, M., Ciccozzi, M., Terrinoni, A., Jiang, W.-C., Wang, C.-B., and Bernardini, S.: The COVID-19 pandemic, *Critical Reviews in Clinical Laboratory Sciences*, 57, 365–388, <https://doi.org/10.1080/10408363.2020.1783198>, <https://doi.org/10.1080/10408363.2020.1783198>, PMID: 32645276, 2020.

- Doms, G. and Schättler, U.: A description of the nonhydrostatic regional model LM, Part I: Dynamics and Numerics, Deutscher Wetterdienst, Offenbach, 2002.
- 525 Erfani, A., Mailhot, J., Gravel, S., Desgagné, M., King, P., Sills, D., McLennan, N., and Jacob, D.: The high resolution limited area version of the Global Environmental Multiscale model and its potential operational applications, 2005.
- Fazzini, M., Cordeschi, M., Carabella, C., Paglia, G., Esposito, G., and Miccadei, E.: Snow Avalanche Assessment in Mass Movement-Prone Areas: Results from Climate Extremization in Relationship with Environmental Risk Reduction in the Prati di Tivo Area (Gran Sasso Massif, Central Italy), *Land*, 10, <https://doi.org/10.3390/land10111176>, <https://www.mdpi.com/2073-445X/10/11/1176>, 2021.
- 530 Frigo, B., Bartelt, P., Chiaia, B., Chiambretti, I., and Maggioni, M.: A Reverse Dynamical Investigation of the Catastrophic Wood-Snow Avalanche of 18 January 2017 at Rigopiano, Gran Sasso National Park, Italy, *International Journal of Disaster Risk Science*, 12, 40–55, 2021.
- Gascoin, S., Hagolle, O., Huc, M., Jarlan, L., Dejoux, J.-F., Szczypta, C., Marti, R., and Sánchez, R.: A snow cover climatology for the Pyrenees from MODIS snow products, *Hydrology and Earth System Sciences*, 19, 2337–2351, [https://doi.org/10.5194/hess-19-2337-](https://doi.org/10.5194/hess-19-2337-2015)
- 535 2015, <https://hess.copernicus.org/articles/19/2337/2015/>, 2015.
- Gerber, F., Besic, N., Sharma, V., Mott, R., Daniels, M., Gabella, M., Berne, A., Germann, U., and Lehning, M.: Spatial variability in snow precipitation and accumulation in COSMO–WRF simulations and radar estimations over complex terrain, *The Cryosphere*, 12, 3137–3160, <https://doi.org/10.5194/tc-12-3137-2018>, <https://tc.copernicus.org/articles/12/3137/2018/>, 2018.
- Grell, G. A. and Freitas, S. R.: A scale and aerosol aware stochastic convective parameterization for weather and air quality modeling, *Atmospheric Chemistry and Physics*, 14, 5233–5250, <https://doi.org/10.5194/acp-14-5233-2014>, [https://acp.copernicus.org/articles/14/](https://acp.copernicus.org/articles/14/5233/2014/)
- 540 5233/2014/, 2014.
- Hall, A.: The Role of Surface Albedo Feedback in Climate, *Journal of Climate*, 17, 1550 – 1568, [https://doi.org/10.1175/1520-0442\(2004\)017<1550:TROSAF>2.0.CO;2](https://doi.org/10.1175/1520-0442(2004)017<1550:TROSAF>2.0.CO;2), https://journals.ametsoc.org/view/journals/clim/17/7/1520-0442_2004_017_1550_trosaf_2.0.co_2.xml, 2004.
- 545 Horton, S. and Jamieson, B.: Modelling hazardous surface hoar layers across western Canada with a coupled weather and snow cover model, *Cold Regions Science and Technology*, 128, 22–31, <https://doi.org/https://doi.org/10.1016/j.coldregions.2016.05.002>, <https://www.sciencedirect.com/science/article/pii/S0165232X16300854>, 2016.
- Horton, S., Schirmer, M., and Jamieson, B.: Meteorological, elevation, and slope effects on surface hoar formation, *The Cryosphere*, 9, 1523–1533, <https://doi.org/10.5194/tc-9-1523-2015>, <https://tc.copernicus.org/articles/9/1523/2015/>, 2015.
- 550 Iacono, M. J., Delamere, J. S., Mlawer, E. J., Shephard, M. W., Clough, S. A., and Collins, W. D.: Radiative forcing by long-lived greenhouse gases: Calculations with the AER radiative transfer models, *Journal of Geophysical Research: Atmospheres*, 113, <https://doi.org/https://doi.org/10.1029/2008JD009944>, <https://agupubs.onlinelibrary.wiley.com/doi/abs/10.1029/2008JD009944>, 2008.
- ISPRA: Valori climatici normali di temperatura e precipitazione in Italia, Stato dell’ambiente 55/2014, http://www.scia.isprambiente.it/wwwrootscia/Documentazione/rapporto_Valori_normali_def.pdf, 2015.
- 555 Italian Civil Protection Department and CIMA Research Foundation: The Dewetra Platform: A Multi-perspective Architecture for Risk Management during Emergencies, in: *Information Systems for Crisis Response and Management in Mediterranean Countries*, edited by Hanachi, C., Bénaben, F., and Charoy, F., pp. 165–177, Springer International Publishing, Cham, 2014.
- Köppen, W.: *Grundriss der klimakunde*, Walter de Gruyter GmbH & Co KG, 1931.

- Koren, V., Schaake, J., Mitchell, K., Duan, Q.-Y., Chen, F., and Baker, J. M.: A parameterization of snowpack and frozen ground intended for NCEP weather and climate models, *Journal of Geophysical Research: Atmospheres*, 104, 19 569–19 585, <https://doi.org/https://doi.org/10.1029/1999JD900232>, <https://agupubs.onlinelibrary.wiley.com/doi/abs/10.1029/1999JD900232>, 1999.
- Lafore, J.-P., Stein, J., Asencio, N., Bougeault, P., Ducrocq, V., Duron, J., Fischer, C., Hérelil, P., Mascart, P., Masson, V., Pinty, J.-P., Redelsperger, J.-L., Richard, E., and Arellano, J.: The Meso-NH Atmospheric Simulation System. Part I: Adiabatic formulation and control simulations, *Annales Geophysicae*, 16, <https://doi.org/10.1007/s005850050582>, 1997.
- 565 Lehning, M., Bartelt, P., Brown, B., and Fierz, C.: A physical SNOWPACK model for the Swiss avalanche warning: Part III: meteorological forcing, thin layer formation and evaluation, *Cold Regions Science and Technology*, 35, 169–184, [https://doi.org/10.1016/S0165-232X\(02\)00072-1](https://doi.org/10.1016/S0165-232X(02)00072-1), 2002a.
- Lehning, M., Bartelt, P., Brown, B., Fierz, C., and Satyawali, P.: A physical SNOWPACK model for the Swiss avalanche warning: Part II. Snow microstructure, *Cold Regions Science and Technology*, 35, 147–167, [https://doi.org/10.1016/S0165-232X\(02\)00073-3](https://doi.org/10.1016/S0165-232X(02)00073-3), 2002b.
- 570 Lehning, M., Völksch, I., Gustafsson, D., Nguyen, T. A., Stähli, M., and Zappa, M.: ALPINE3D: a detailed model of mountain surface processes and its application to snow hydrology, *Hydrological Processes*, 20, 2111–2128, <https://doi.org/https://doi.org/10.1002/hyp.6204>, <https://onlinelibrary.wiley.com/doi/abs/10.1002/hyp.6204>, 2006.
- Lehning, M., Löwe, H., Rysler, M., and Raderschall, N.: Inhomogeneous precipitation distribution and snow transport in steep terrain, *Water Resources Research*, 44, <https://doi.org/https://doi.org/10.1029/2007WR006545>, <https://agupubs.onlinelibrary.wiley.com/doi/abs/10.1029/2007WR006545>, 2008.
- 575 Lena, B., Antenucci, F., and Mariani, L.: Space and time evolution of the Abruzzo precipitation, *Italian Journal of Agrometeorology*, pp. 5–20, 2012.
- Libertino, A., Ganora, D., and Claps, P.: Technical note: Space–time analysis of rainfall extremes in Italy: clues from a reconciled dataset, *Hydrology and Earth System Sciences*, 22, 2705–2715, <https://doi.org/10.5194/hess-22-2705-2018>, <https://hess.copernicus.org/articles/22/2705/2018/>, 2018.
- 580 Livneh, B., Xia, Y., Mitchell, K. E., Ek, M. B., and Lettenmaier, D. P.: Noah LSM Snow Model Diagnostics and Enhancements, *Journal of Hydrometeorology*, 11, 721 – 738, <https://doi.org/10.1175/2009JHM1174.1>, https://journals.ametsoc.org/view/journals/hydr/11/3/2009jhm1174_1.xml, 2010.
- Longobardi, A. and Villani, P.: Trend analysis of annual and seasonal rainfall time series in the Mediterranean area, *International Journal of Climatology*, 30, 1538–1546, <https://doi.org/https://doi.org/10.1002/joc.2001>, <https://rmets.onlinelibrary.wiley.com/doi/abs/10.1002/joc.2001>, 2010.
- 585 Luitjing, H., Vikhamar-Schuler, D., Aspelien, T., Bakketun, Å., and Homleid, M.: Forcing the SURFEX/Crocus snow model with combined hourly meteorological forecasts and gridded observations in southern Norway, *The Cryosphere*, 12, 2123–2145, <https://doi.org/10.5194/tc-12-2123-2018>, <https://tc.copernicus.org/articles/12/2123/2018/>, 2018.
- 590 Lussana, C., Saloranta, T., Skaugen, T., Magnusson, J., Tveito, O. E., and Andersen, J.: seNorge2 daily precipitation, an observational gridded dataset over Norway from 1957 to the present day, *Earth System Science Data*, 10, 235–249, <https://doi.org/10.5194/essd-10-235-2018>, <https://essd.copernicus.org/articles/10/235/2018/>, 2018a.
- Lussana, C., Tveito, O. E., and Uboldi, F.: Three-dimensional spatial interpolation of 2 m temperature over Norway, *Quarterly Journal of the Royal Meteorological Society*, 144, 344–364, <https://doi.org/https://doi.org/10.1002/qj.3208>, <https://rmets.onlinelibrary.wiley.com/doi/abs/10.1002/qj.3208>, 2018b.
- 595

- Mailhot, J., Bélair, S., Lefavre, L., Bilodeau, B., Desgagné, M., Girard, C., Glazer, A., Leduc, A., Méthot, A., Patoine, A., Plante, A., Rahill, A., Robinson, T., Talbot, D., Tremblay, A., Vaillancourt, P., Zadra, A., and Qaddouri, A.: The 15-km version of the Canadian regional forecast system, *Atmosphere-Ocean*, 44, 133–149, <https://doi.org/10.3137/ao.440202>, <https://doi.org/10.3137/ao.440202>, 2006.
- 600 Marsh, C. B., Pomeroy, J. W., Spiteri, R. J., and Wheeler, H. S.: A Finite Volume Blowing Snow Model for Use With Variable Resolution Meshes, *Water Resources Research*, 56, e2019WR025307, <https://doi.org/https://doi.org/10.1029/2019WR025307>, <https://agupubs.onlinelibrary.wiley.com/doi/abs/10.1029/2019WR025307>, e2019WR025307 2019WR025307, 2020a.
- Marsh, C. B., Pomeroy, J. W., and Wheeler, H. S.: The Canadian Hydrological Model (CHM) v1.0: a multi-scale, multi-extent, variable-complexity hydrological model – design and overview, *Geoscientific Model Development*, 13, 225–247, <https://doi.org/10.5194/gmd-13-225-2020>, <https://gmd.copernicus.org/articles/13/225/2020/>, 2020b.
- 605 Metsämäki, S., Mattila, O.-P., Pulliainen, J., Niemi, K., Luojus, K., and Böttcher, K.: An optical reflectance model-based method for fractional snow cover mapping applicable to continental scale, *Remote Sensing of Environment*, 123, 508 – 521, <https://doi.org/https://doi.org/10.1016/j.rse.2012.04.010>, <http://www.sciencedirect.com/science/article/pii/S0034425712001794>, 2012.
- Milbrandt, J. A., Bélair, S., Faucher, M., Vallée, M., Carrera, M. L., and Glazer, A.: The Pan-Canadian High Resolution (2.5 km) Deterministic Prediction System, *Weather and Forecasting*, 31, 1791 – 1816, <https://doi.org/10.1175/WAF-D-16-0035.1>, https://journals.ametsoc.org/view/journals/wefo/31/6/waf-d-16-0035_1.xml, 2016.
- Ministero dei Lavori Pubblici: Carta della precipitazione nevosa media annua in Italia nel quarantennio 1921-1960: tavola rotonda della geografia della neve in Italia : Roma, 28-29 Maggio 1973, <https://books.google.it/books?id=QkCdoAEACAAJ>, 1973.
- Mott, R., Vionnet, V., and Grünwald, T.: The Seasonal Snow Cover Dynamics: Review on Wind-Driven Coupling Processes, *Frontiers in Earth Science*, 6, <https://doi.org/10.3389/feart.2018.00197>, <https://www.frontiersin.org/articles/10.3389/feart.2018.00197>, 2018.
- 615 Müller, M., Homleid, M., Ivarsson, K.-I., Koltzow, M. A. O., Lindskog, M., Midtbø, K. H., Andrae, U., Aspelién, T., Berggren, L., Bjorge, D., Dahlgren, P., Kristiansen, J., Randriamampianina, R., Ridal, M., and Vignes, O.: AROME-MetCoOp: A Nordic Convective-Scale Operational Weather Prediction Model, *Weather and Forecasting*, 32, 609 – 627, <https://doi.org/10.1175/WAF-D-16-0099.1>, https://journals.ametsoc.org/view/journals/wefo/32/2/waf-d-16-0099_1.xml, 2017.
- 620 Nurmi, P.: Recommendations on the verification of local weather forecasts., p. 19, <https://doi.org/10.21957/y1z1thg51>, <https://www.ecmwf.int/node/11401>, 2003.
- Pavan, V., Tomozeiu, R., Cacciamani, C., and Di Lorenzo, M.: Daily precipitation observations over Emilia-Romagna: mean values and extremes, *International Journal of Climatology*, 28, 2065–2079, <https://doi.org/https://doi.org/10.1002/joc.1694>, <https://rmets.onlinelibrary.wiley.com/doi/abs/10.1002/joc.1694>, 2008.
- 625 Pavelsky, T. M., Kapnick, S., and Hall, A.: Accumulation and melt dynamics of snowpack from a multiresolution regional climate model in the central Sierra Nevada, California, *Journal of Geophysical Research: Atmospheres*, 116, <https://doi.org/https://doi.org/10.1029/2010JD015479>, <https://agupubs.onlinelibrary.wiley.com/doi/abs/10.1029/2010JD015479>, 2011.
- Petriccione, B. and Bricca, A.: Thirty years of ecological research at the Gran Sasso d’Italia LTER site: Climate change in action, *Nature Conservation*, 34, 9–39, <https://doi.org/10.3897/natureconservation.34.30218>, 2019.
- 630 Piacentini, T., Calista, M., Crescenti, U., Miccadei, E., and Sciarra, N.: Seismically Induced Snow Avalanches: The Central Italy Case, *Frontiers in Earth Science*, 8, 507, <https://doi.org/10.3389/feart.2020.599611>, <https://www.frontiersin.org/article/10.3389/feart.2020.599611>, 2020.
- Pinna, M.: Contributo alla classificazione del clima d’Italia, *Rivista Geografica Italiana*, 77, 129–152, 1970.

- Quéno, L., Vionnet, V., Dombrowski-Etchevers, I., Lafaysse, M., Dumont, M., and Karbou, F.: Snowpack modelling in the Pyrenees driven
635 by kilometeric resolution meteorological forecasts, *The Cryosphere*, 10, 1571–1589, <https://doi.org/10.5194/tc-10-1571-2016>, <https://tc.copernicus.org/articles/10/1571/2016/>, 2016.
- Rapisarda, A. and Pranzo, A. M. R.: Mapping the avalanche risk: from survey to cartographic production. The avalanche bulletin of the
Meteomont Service of the Alpine Troops Command, in: *Proceedings of the ICA*, vol. 4, p. 92, Copernicus GmbH, 2021.
- Romano, E. and Preziosi, E.: Precipitation pattern analysis in the Tiber River basin (central Italy) using standardized indices, *International
640 Journal of Climatology*, 33, 1781–1792, <https://doi.org/https://doi.org/10.1002/joc.3549>, <https://rmets.onlinelibrary.wiley.com/doi/abs/10.1002/joc.3549>, 2013.
- Romeo, V. and Massimiliano, F.: La neve in Appennino. Prime analisi su 30 anni di dati meteorologici., *Neve e Valanghe*, 63, <https://issuu.com/aineva7/docs/nv63>, 2008.
- Rossi, G.: *Institutional Framework of Water Governance*, pp. 83–100, Springer International Publishing, Cham, https://doi.org/10.1007/978-3-030-36460-1_4,
645 https://doi.org/10.1007/978-3-030-36460-1_4, 2020.
- Schirmer, M. and Jamieson, B.: Verification of analysed and forecasted winter precipitation in complex terrain, *The Cryosphere*, 9, 587–601,
<https://doi.org/10.5194/tc-9-587-2015>, <https://tc.copernicus.org/articles/9/587/2015/>, 2015.
- Scorzini, A. R. and Leopardi, M.: Precipitation and temperature trends over central Italy (Abruzzo Region): 1951–2012, *Theoretical and
applied climatology*, 135, 959–977, https://doi.org/https://doi.org/10.1007/978-3-030-36460-1_4, 2019.
- 650 Seity, Y., Brousseau, P., Malardel, S., Hello, G., B?nard, P., Bouttier, F., Lac, C., and Masson, V.: The AROME-France Convective-Scale
Operational Model, *Monthly Weather Review*, 139, 976 – 991, <https://doi.org/10.1175/2010MWR3425.1>, <https://journals.ametsoc.org/view/journals/mwre/139/3/2010mwr3425.1.xml>, 2011.
- Sharma, V., Gerber, F., and Lehning, M.: Introducing CRYOWRF v1. 0: Multiscale atmospheric flow simulations with advanced snow cover
modelling, *Geoscientific Model Development Discussions*, pp. 1–46, <https://doi.org/https://doi.org/10.5194/gmd-2021-231>, 2021.
- 655 Skamarock, W. C., Klemp, J. B., Dudhia, J., Gill, D. O., Liu, Z., Berner, J., Wang, W., Powers, J. G., Duda, M. G., Barker, D. M., et al.:
A description of the advanced research WRF model version 3, National Center for Atmospheric Research: Boulder, CO, USA, p. 145,
<https://doi.org/http://dx.doi.org/10.5065/D68S4MVH>, 2008.
- Sommer, C. G., Lehning, M., and Fierz, C.: Wind Tunnel Experiments: Influence of Erosion and Deposition on Wind-Packing of New Snow,
Frontiers in Earth Science, 6, 4, <https://doi.org/10.3389/feart.2018.00004>, <https://www.frontiersin.org/article/10.3389/feart.2018.00004>,
660 2018.
- Thompson, G., Field, P. R., Rasmussen, R. M., and Hall, W. D.: Explicit Forecasts of Winter Precipitation Using an Improved Bulk
Microphysics Scheme. Part II: Implementation of a New Snow Parameterization, *Monthly Weather Review*, 136, 5095 – 5115,
<https://doi.org/10.1175/2008MWR2387.1>, <https://journals.ametsoc.org/view/journals/mwre/136/12/2008mwr2387.1.xml>, 2008.
- Vanat, L.: *International Report on Snow & Mountain Tourism*, <https://www.vanat.ch/RM-world-report-2020.pdf>, 2020.
- 665 Vionnet, V., Brun, E., Morin, S., Boone, A., Faroux, S., Le Moigne, P., Martin, E., and Willemet, J.-M.: The detailed snowpack scheme
Crocus and its implementation in SURFEX v7.2, *Geoscientific Model Development*, 5, 773–791, <https://doi.org/10.5194/gmd-5-773-2012>,
<https://gmd.copernicus.org/articles/5/773/2012/>, 2012.
- Vionnet, V., Dombrowski-Etchevers, I., Lafaysse, M., Qu?no, L., Seity, Y., and Bazile, E.: Numerical Weather Forecasts at Kilometer
Scale in the French Alps: Evaluation and Application for Snowpack Modeling, *Journal of Hydrometeorology*, 17, 2591 – 2614,
670 <https://doi.org/10.1175/JHM-D-15-0241.1>, https://journals.ametsoc.org/view/journals/hydr/17/10/jhm-d-15-0241_1.xml, 2016.

- Vionnet, V., Martin, E., Masson, V., Lac, C., Naaim Bouvet, F., and Guyomarc'h, G.: High-Resolution Large Eddy Simulation of Snow Accumulation in Alpine Terrain, *Journal of Geophysical Research: Atmospheres*, 122, 11,005–11,021, <https://doi.org/https://doi.org/10.1002/2017JD026947>, <https://agupubs.onlinelibrary.wiley.com/doi/abs/10.1002/2017JD026947>, 2017.
- 675 Vionnet, V., Marsh, C. B., Menounos, B., Gascoïn, S., Wayand, N. E., Shea, J., Mukherjee, K., and Pomeroy, J. W.: Multi-scale snowdrift-permitting modelling of mountain snowpack, *The Cryosphere*, 15, 743–769, <https://doi.org/10.5194/tc-15-743-2021>, <https://tc.copernicus.org/articles/15/743/2021/>, 2021.
- Wang, Z., Zeng, X., and Decker, M.: Improving snow processes in the Noah land model, *Journal of Geophysical Research: Atmospheres*, 115, <https://doi.org/https://doi.org/10.1029/2009JD013761>, <https://agupubs.onlinelibrary.wiley.com/doi/abs/10.1029/2009JD013761>, 2010.
- 680 Wever, N., Fierz, C., Mitterer, C., Hirashima, H., and Lehning, M.: Solving Richards Equation for snow improves snowpack meltwater runoff estimations in detailed multi-layer snowpack model, *The Cryosphere*, 8, 257–274, <https://doi.org/10.5194/tc-8-257-2014>, <https://tc.copernicus.org/articles/8/257/2014/>, 2014.

List of TABLES

Table 1. Number of stations and observations for each of the analysed variables at different elevation bands.

	Number of stations - observations			
	Low elevation (< 800 m)	Mid elevation (800-1600 m)	High elevation (\geq 1600 m)	Total
Air temperature	295 - 1830864	55 - 317856	7 - 39528	357 - 2188248
Relative humidity	116- 677016	15 - 69528	6 - 33480	137 - 780024
Wind speed	52 - 322320	10 - 49872	7 - 39288	69 - 411480
Incoming shortwave radiation	29 - 173376	6 - 15936	5 - 19200	40 - 208512
Precipitation	363 - 887448	54 - 142392	4 - 8280	384 - 1038120
Snow height	0 - 0	36 - 161544	4 - 15912	40 - 177456
Snow water equivalent	0 - 0	24 - 92232	3 - 9336	27 - 101568

Table 2. Number of snow stations for different elevation bands

Elevation bands (m a.s.l.)	Number of stations
750-1000	3
1000-1250	9
1250-1500	21
1500-1750	6
1750-2000	0
2000-2250	1

Table 3. WRF mean bias error (MBE), mean absolute error (MAE) and correlation coefficient (R) of air temperature, relative humidity, wind speed, incoming shortwave radiation and daily precipitation, for low elevation (< 800 m), mid elevation (800-1600 m) and high elevation (\geq 1600 m) bands.

	Low elevation (< 800 m)			Mid elevation (800-1600 m)			High elevation (\geq 1600 m)			All		
	MBE	MAE	R	MBE	MAE	R	MBE	MAE	R	MBE	MAE	R
Air temperature ($^{\circ}$ C)	-0.32	1.45	0.89	-1.45	1.99	0.9	-0.23	1.68	0.89	-0.52	1.56	0.9
Relative humidity (%)	0.19	8.92	0.68	5.57	9.77	0.78	11.54	14.63	0.76	2.02	9.38	0.68
Wind speed (ms^{-1})	1.11	1.37	0.66	-0.99	1.67	0.64	-2.17	3.32	0.39	0.53	1.59	0.49
Incoming shortwave radiation (Wm^{-2})	58.3	71.2	0.86	64.9	77.8	0.84	61.6	100.9	0.69	59.1	74.3	0.85
Daily precipitation (mm)	0.44	4.23	0.77	1.14	5.42	0.76	4.28	7.39	0.64	0.61	4.38	0.77

Table 4. WRF-Noah and WRF-Alpine3D mean bias error (MBE), mean absolute error (MAE) and correlation coefficient (R) for simulated snow height, daily snow height variation and snow water equivalent.

	Snow height (cm)			Daily snow height variation (cm)			Snow water equivalent (kgm ⁻²)		
	MBE	MAE	R	MBE	MAE	R	MBE	MAE	R
WRF-Noah	-3.9	13.8	0.68	-0.06	2.9	0.64	-41.6	66.6	0.47
WRF-Alpine3D	5.8	12.4	0.87	0.05	2.8	0.63	34.5	67.6	0.74

Table 5. WRF-Noah and WRF-Alpine3D mean bias error (MBE), mean absolute error (MAE) and correlation coefficient (R) for simulated snow cover area fractions.

	Snow cover area fraction		
	MBE	MAE	R
WRF-Noah	0.06	0.06	0.89
WRF-Alpine3D	0.06	0.06	0.88

Table 6. Mean values of Jaccard index and Average Symmetric Surface Distance for WRF-Noah and WRF-Alpine3D.

	J	ASSD
WRF-Noah	0.3	2.3
WRF-Alpine3D	0.3	2.3

List of FIGURES

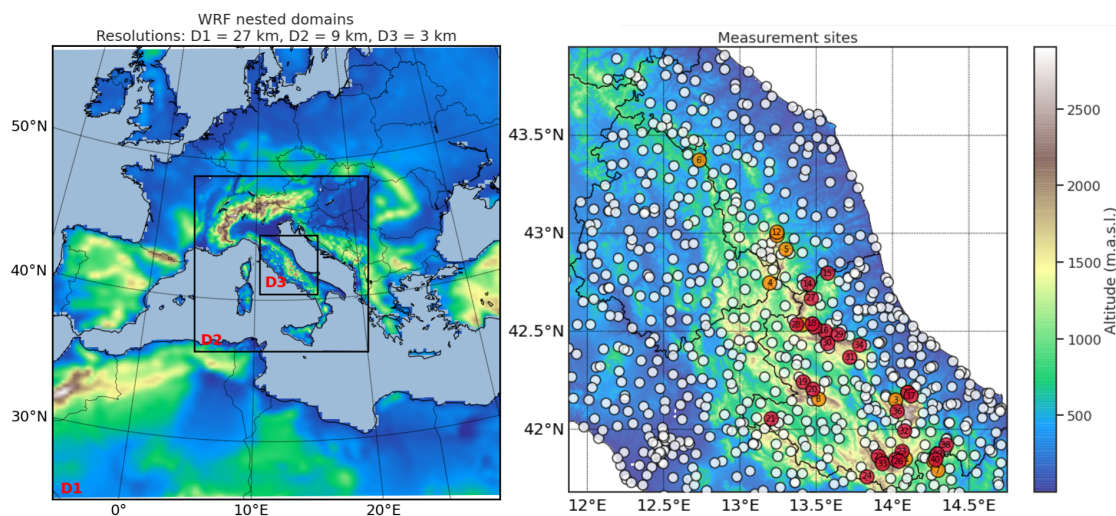


Figure 1. a) WRF nested domains D1, D2 and D3 with resolution 27 km, 9 km, 3 km respectively. b) Atmospheric and snow measurement site locations in the D3 domain. The white circles represent automatic weather stations without snow height sensor, while orange and red circles represents automatic weather stations with snow height sensor and manual measurement sites respectively.

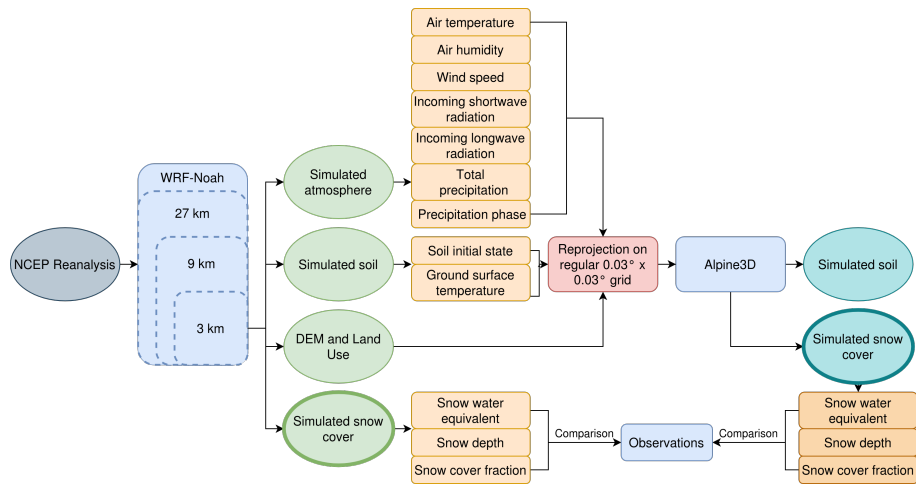


Figure 2. Flowchart of the model chain realized in this study. NCEP reanalyses are used to initialize the WRF model, which provides the atmospheric forcing data to drive WRF-Noah (online coupled) and WRF-Alpine3D (offline coupled) numerical models.

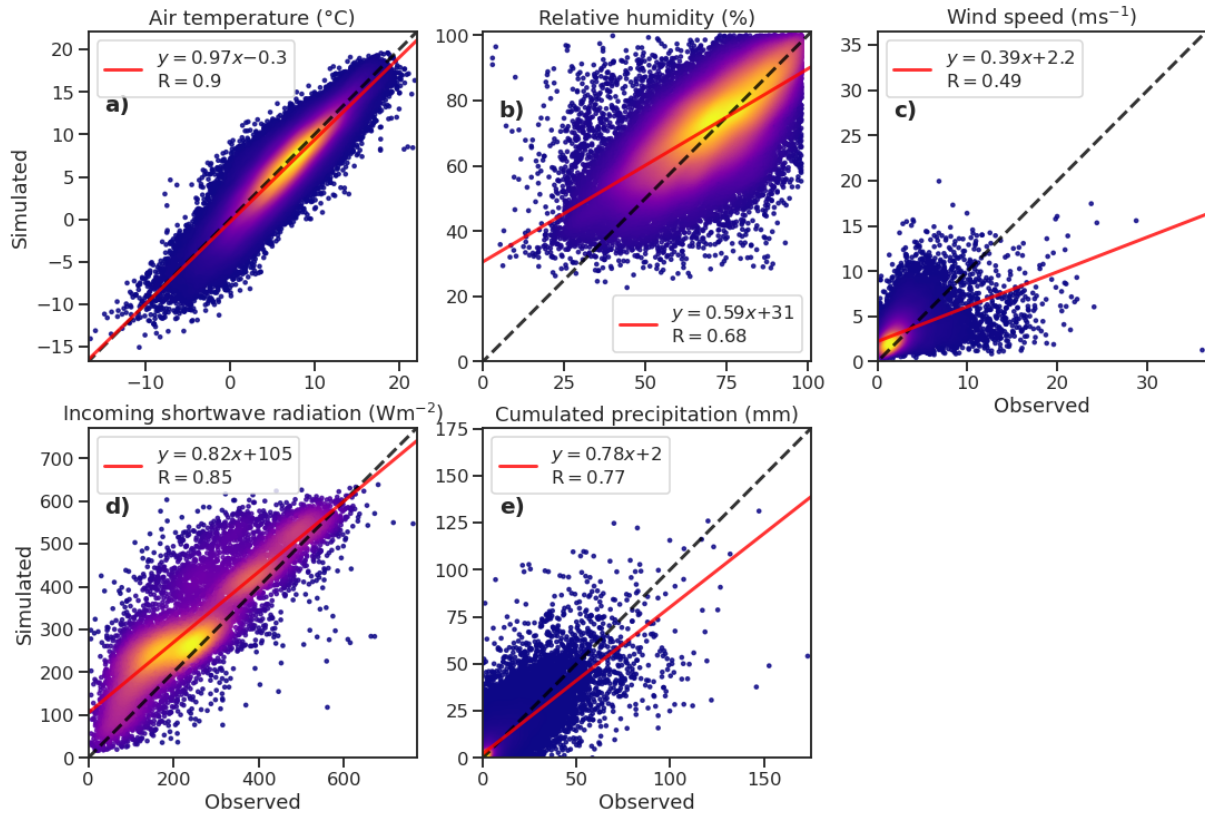


Figure 3. Comparison of in situ observed data and WRF simulations of daily air temperature (a), relative humidity (b), wind speed (c), incoming shortwave radiation (d) and precipitation (e). The density of observations for each pixel of the plot is represented with a color, the brighter is the color, the higher is the density of observations for that pixel.

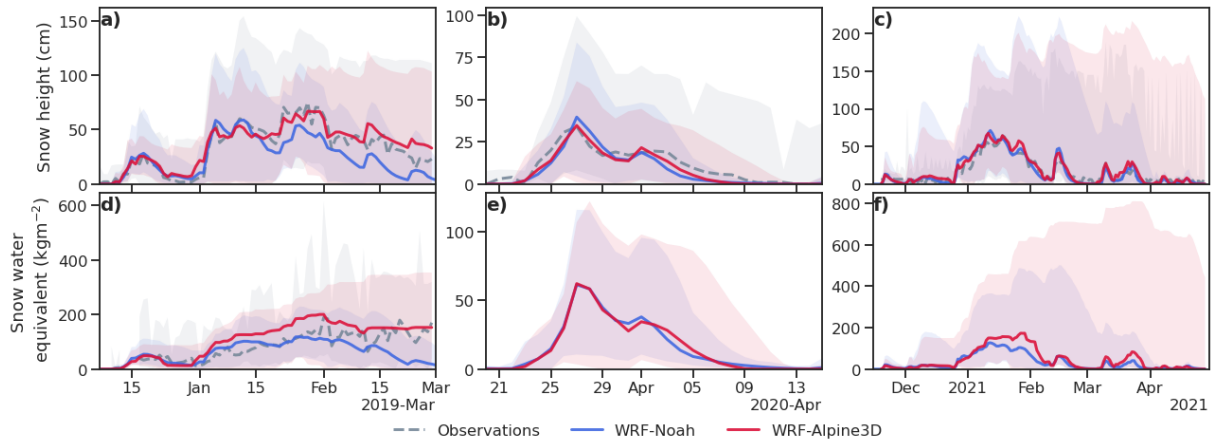


Figure 4. Time series of observed and simulated snow height (first row) and snow water equivalent (second row). Solid lines represent the median of all available stations for each considered year: observations are indicated by a solid gray line, while simulations are indicated by solid blue and red lines, corresponding to WRF-Noah and WRF-Alpine3D, respectively. The shaded areas correspond to the maximum and minimum snow height and snow water equivalent observed or simulated. The low temporal frequency of the manual measurements for winter 2020 and 2021, and the non contemporaneity of the observations at different sites make the timeseries of the median of the observed snow water equivalent noisy and uninformative, thus we decided to not show it in figures e) and f).

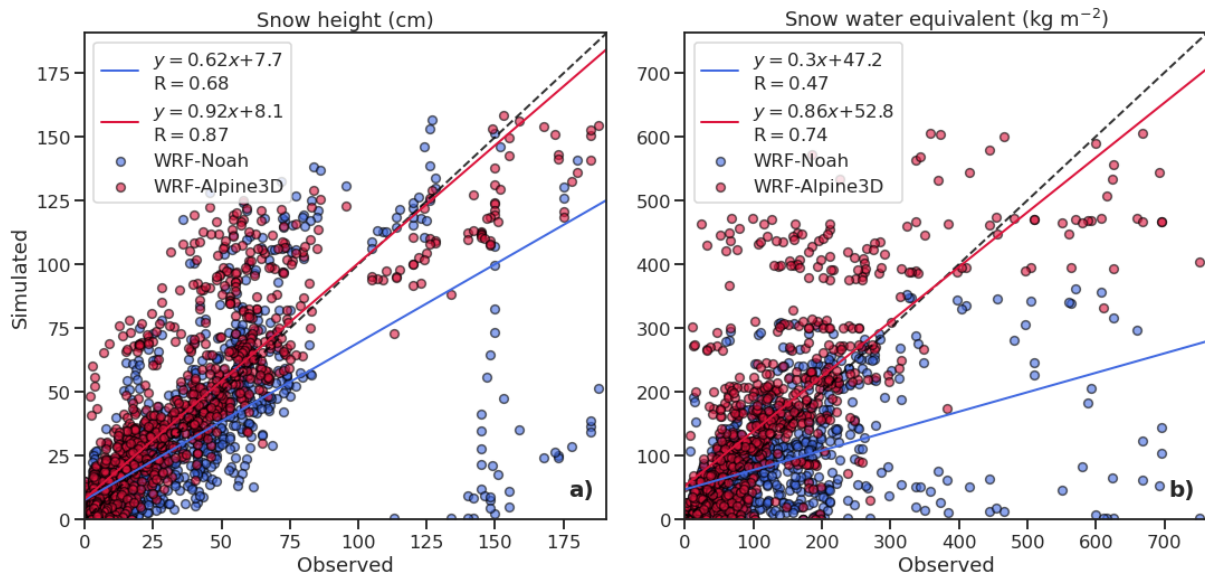


Figure 5. Comparison of simulated and measured daily means of snow height (a) and snow water equivalent (b) averaged for each elevation band shown in Table 2. Blue and red dots indicate WRF-Noah and WRF-Alpine3D, respectively. The blue and red lines represent the best linear fit of WRF-Noah and WRF-Alpine3D data.

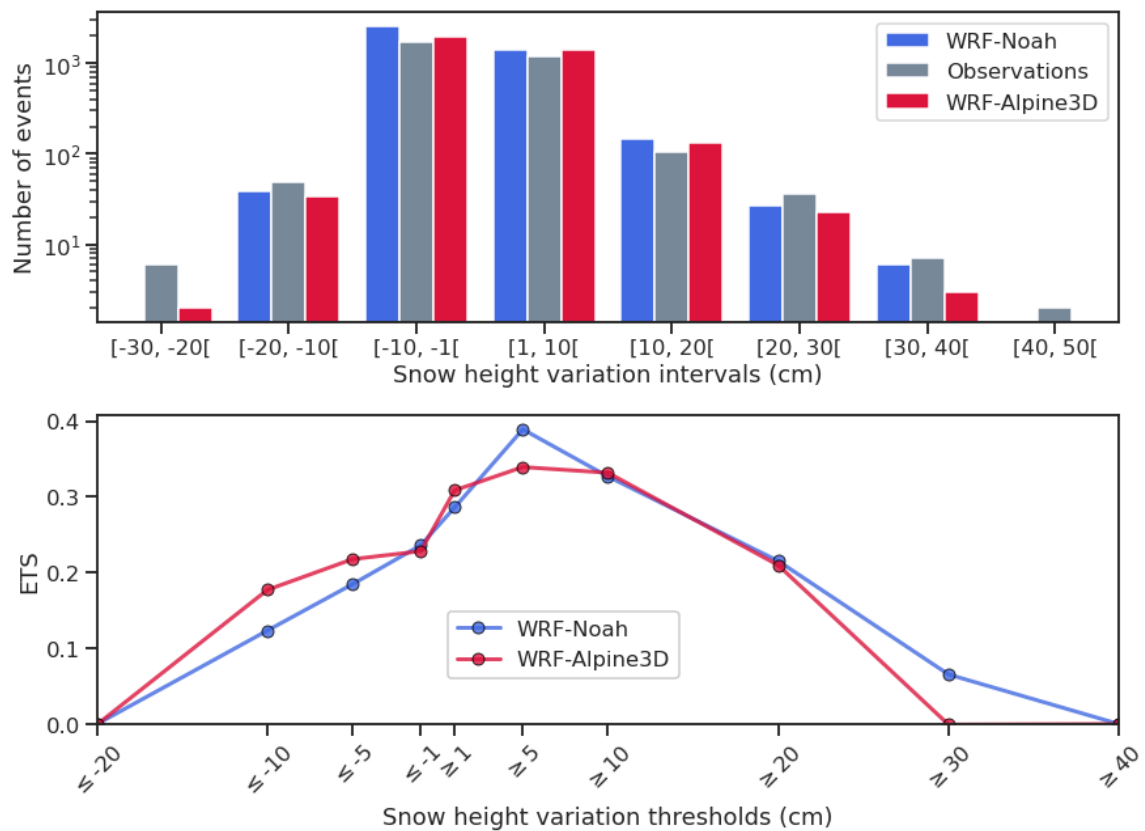


Figure 6. a) Observed and modelled frequency distribution of daily snow height variation obtained from the 13 AWS used in this study. The grey column represents the observed variations and the blue and red columns represent the snow height variations simulated with WRF-Noah and WRF-Alpine3D, respectively. b) ETS index for different snow thresholds with blue and red lines indicating WRF-Noah and WRF-Alpine3D scores, respectively.

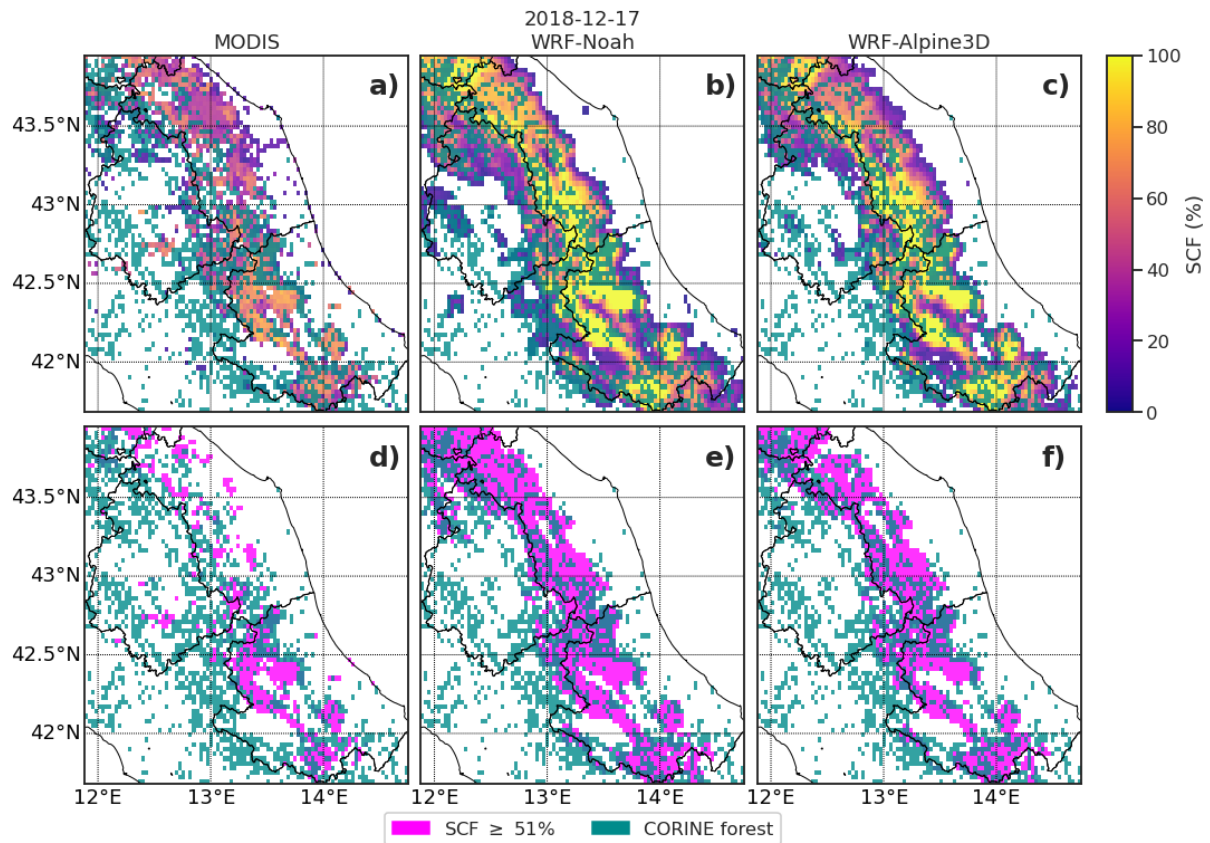


Figure 7. a), b) and c): MODIS, WRF-Noah and WRF-Alpine3D snow cover fraction maps. d), e) and f): MODIS, WRF-Noah and WRF-Alpine3D snow cover area maps derived by applying a threshold of 51% to the corresponding snow cover fraction maps. CORINE broad leaved forest, coniferous forest, and mixed forest classes aggregated and reprojected from original 100 m resolution to 3 km resolution are also shown.

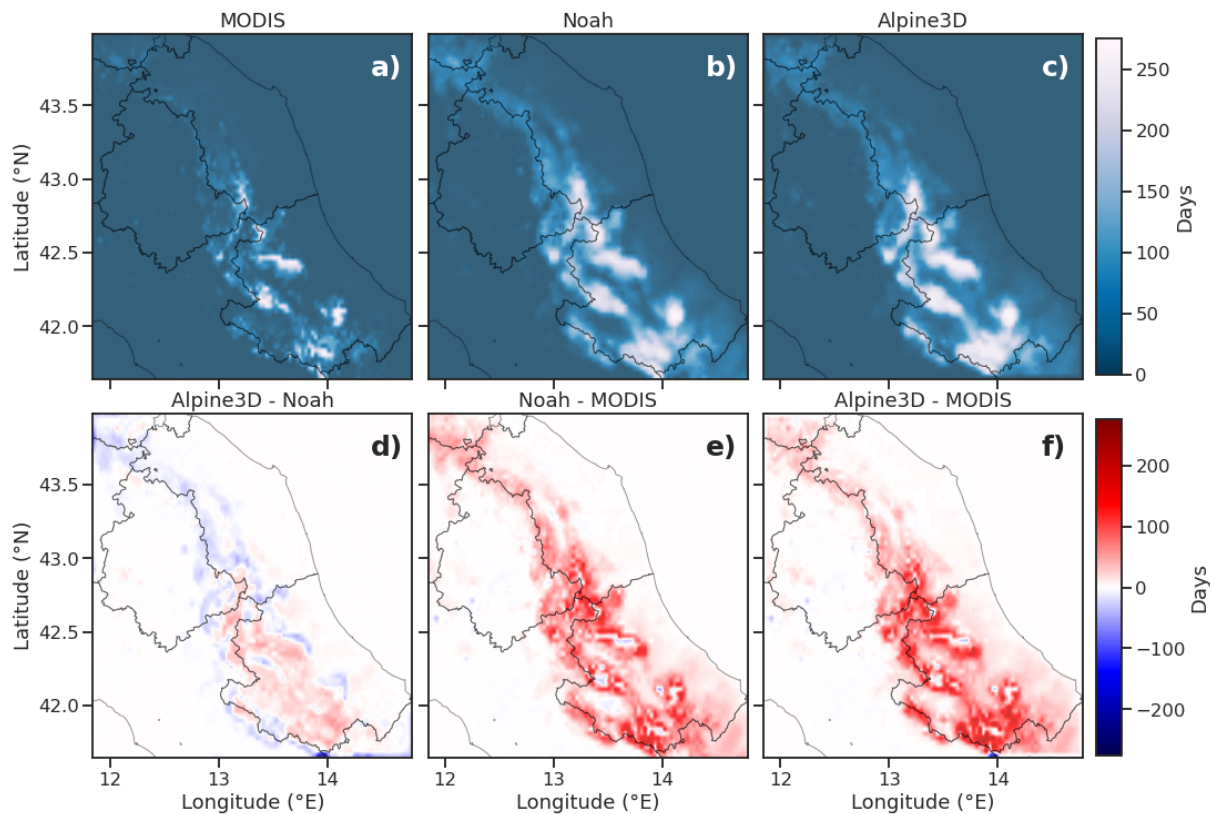


Figure 8. a), b) and c): MODIS, WRF-Noah and WRF-Alpine3D snow cover duration maps derived from snow cover area maps. Fig. d) shows the differences of snow cover duration between WRF-Alpine3D and WRF-Noah, whereas Figs. e) and f) show the differences with MODIS of WRF-Noah and WRF-Alpine3D, respectively.

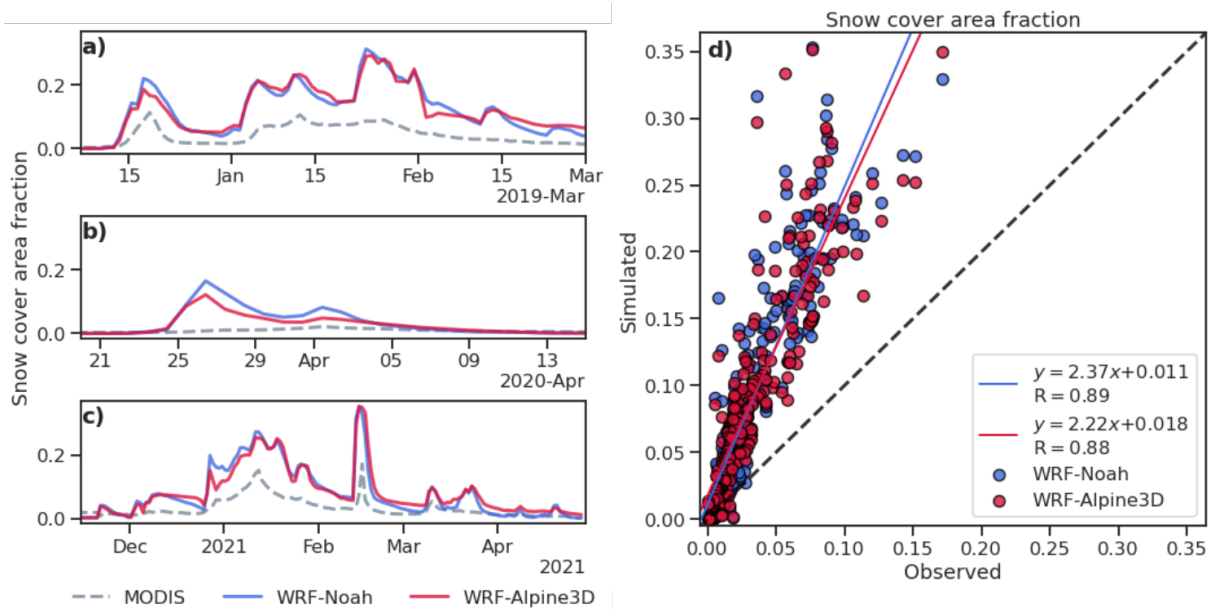


Figure 9. a), b), c): Time series of snow cover area fraction derived from MODIS (grey line), WRF-Noah (blue line) and WRF-Alpine3D (red line) for all selected winters. d) Comparison of simulated and observed snow cover area fraction with blue and red dots indicating WRF-Noah and WRF-Alpine3D, respectively. The blue and red lines represent the best linear fit of WRF-Noah and WRF-Alpine3D data.

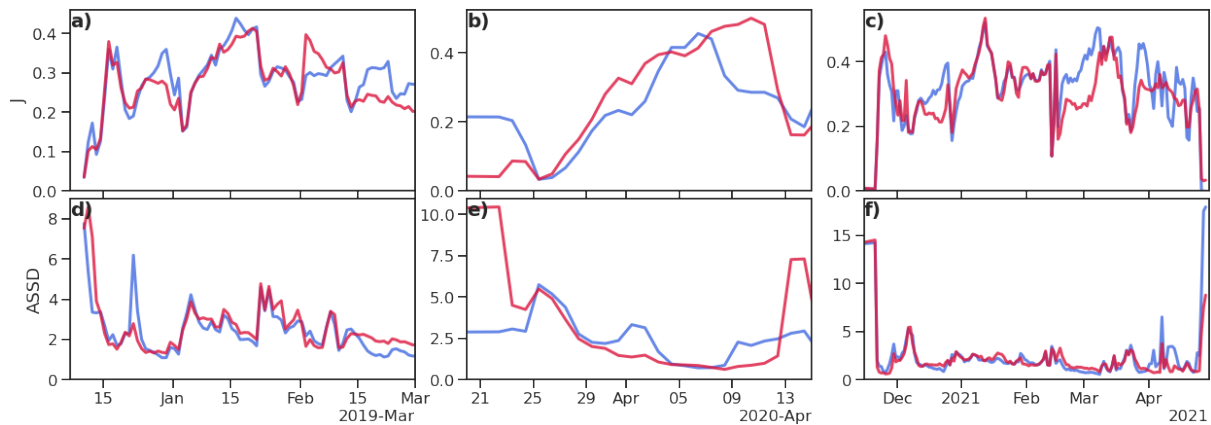


Figure 10. Time series of Jaccard index (first row) and Average Symmetric Surface Distance index (second row) computed for WRF-Noah (red line) and WRF-Alpine3D (blue line) over the selected winters.